# Structure of a Low-Level Jet over Lower Cook Inlet, Alaska*

S. ALLEN MACKLIN

*Pacific Marine Environmental Laboratory, National Oceanic and Atmospheric Administration, Seattle, Washington*

NICHOLAS A. BOND

*Joint Institute for the Study of the Atmosphere and Ocean, University of Washington/NOAA, Seattle, Washington*

JEFFREY P. WALKER**

*Northwest Ocean Service Center/NOAA, Seattle, Washington*

(Manuscript received 31 January 1990, in final form 29 May 1990)

ABSTRACT

During February 1982 a NOAA research aircraft investigated a cold, low-level jet blowing from a gap between mountain ranges on the west side of Cook Inlet, Alaska. The jet blew 200 km southeastward across Cook Inlet between the Kenai Peninsula and the Kodiak archipelago, passing into the Gulf of Alaska where it merged with the large-scale marine wind field. Measurement commenced ~35 km downstream of the seaward end of the gap. The jet's internal boundary layer accelerated by 5% and grew 20% in depth for ~50 km; thereafter, wind speed and boundary-layer depth were nearly constant for the next 100 km. The strongest winds (>20 m $s^{-1}$ at a height of 80 m) were observed on the south side of the jet's thermal axis and 90 km downstream from the coast. Budget analyses reveal that the down-gradient acceleration within the jet was principally opposed by surface friction, and the cold air advection was balanced by a strong upward-directed sensible heat flux from Cook Inlet and entrainment of warmer air from aloft.

## 1. Introduction

Marine weather forecasting for coastal regions presents special problems relating to thermal and orographic discontinuities. This report presents observations of a low-level jet of cold air blowing between the Aleutian and Alaska mountain ranges and crossing lower Cook Inlet, Alaska (Fig. 1a). The high wind speeds and gradients associated with this type of jet create hazardous conditions for mariners and aviators. We discuss the magnitude, orientation, and spatial extent of the jet and its relationship to the large-scale weather pattern, and we present estimates of the mechanisms influencing the downstream evolution of the flow. In general, the results presented here apply to other coastal regions with similar orography.

The jet in question bears similarities to gap winds observed over the Strait of Juan de Fuca (Reed 1931; Overland and Walter 1981), the Strait of Gibraltar (Scorer 1952), and Shelikof Strait (Macklin et al. 1984; Lackmann and Overland 1989). For those studies a gap wind is defined as a flow of air accelerating under the influence of an imposed synoptic-scale pressure gradient parallel to the axis of a sea level channel. However, the flow in this case originated as a mountain-gap wind (Huschke 1959). In that regard it differs from gap winds in sea level channels (Overland 1984) because of the gravitational acceleration associated with the seaward-sloping terrain upstream and the lack of a well-defined channel downstream. Some similarities to fall or bora winds (Smith 1987, among others) may be expected. By necessity we do not study the wind within the gap nor the lower tropospheric structure over the Alaska Peninsula, but rather examine the downstream evolution of the flow over Cook Inlet.

## 2. Geographic setting

Cook Inlet (Fig. 1b) is a complex estuary of the Gulf of Alaska. The northern part, ice covered in winter, serves as a drainage field for cold continental air from the mountainous regions surrounding the city of Anchorage. Lower Cook Inlet contains two large bays: Kachemak Bay to the east drains air from the glaciers of the Kenai Peninsula while to the west Kamishak Bay connects (via the Kamishak gap) Cook Inlet to

* Contribution No. 832 from NOAA/Pacific Marine Environmental Laboratory.

** Present affiliation: NWS, Western Region Headquarters/NOAA, Salt Lake City, Utah.

*Corresponding author address:* Mr. S. Allen Macklin, NOAA/PMEL, 7600 Sand Point Way N. E. Bin C15700, Seattle, WA 98115-0070.

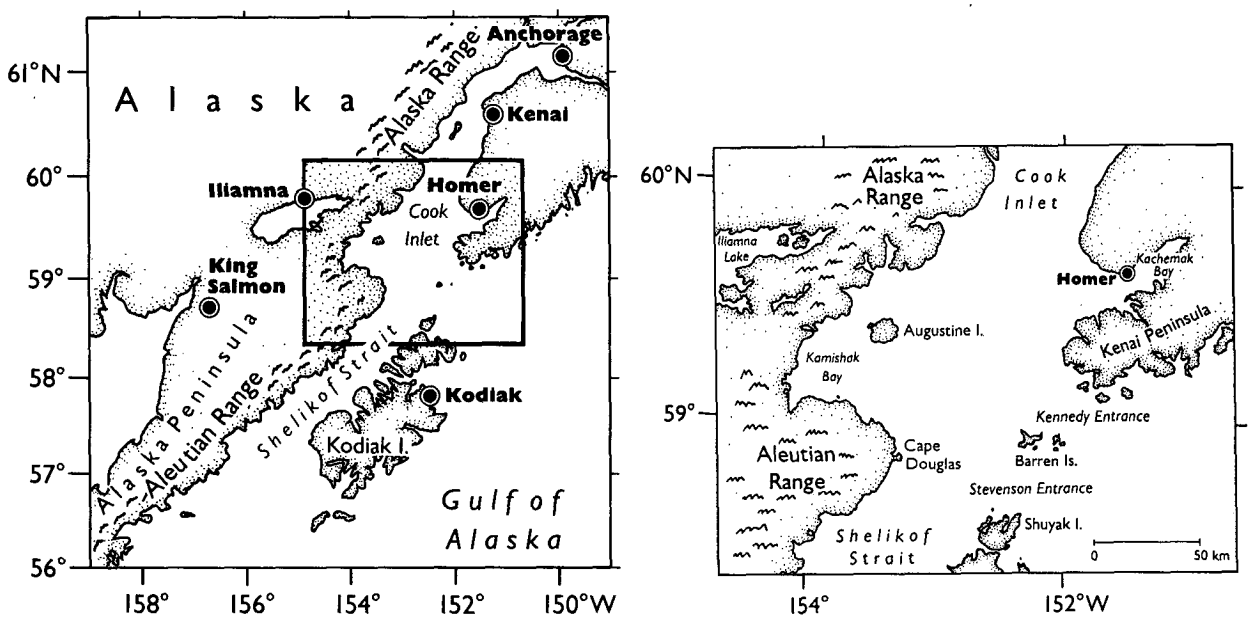


FIG. 1. (a) Cook Inlet and the Alaska Peninsula: the Aleutian Range lies along the east coast of the Alaska Peninsula and the Alaska Range begins on the east coast of Cook Inlet; a break in these mountain ranges occurs southeast of Iliamna. (b) Lower Cook Inlet: the Kamishak gap runs from southeastern Iliamna Lake to Kamishak Bay.

the Iliamna Lake territory. Cook Inlet is joined on the south to Shelikof Strait, which divides the mountainous Kodiak archipelago from the Alaska Peninsula, and is joined on the southeast to the Gulf of Alaska at Kennedy and Stevenson Entrances. Local orography (Fig. 2) suggests two dominant, orthogonal wind channels that intersect over lower Cook Inlet. The north–south channel is formed by upper Cook Inlet and Shelikof Strait; the east–west channel is comprised of Kamishak Gap, Kamishak Bay, and Kennedy and Stevenson Entrances. Flow conditions at the intersection of the channels are reported by Macklin et al. (1980). They found that Cook Inlet winds respond predictably to the large-scale atmospheric pressure field, but with important modifications caused by orography.

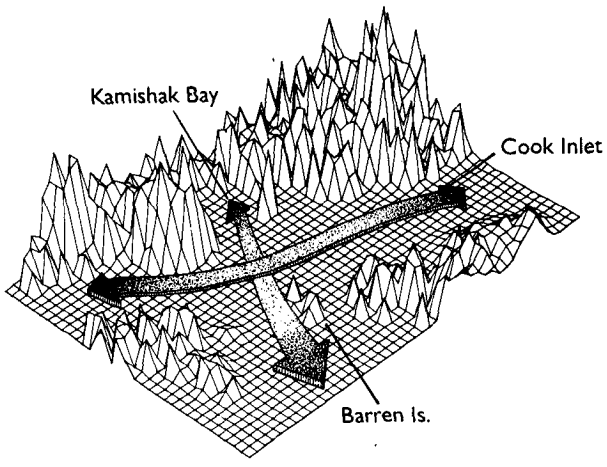


FIG. 2. Orography of lower Cook Inlet: grid spacing is about 6 km, the vertical scale is exaggerated 40-fold. Arrows denote orographic wind channels.

Local mariners and aviators speak of "williwaws and water spouts" along the cliffs of the head waters of Kamishak Bay. These phenomena are associated with strong westerlies funneled through the gap in the mountains between Iliamna Lake and Kamishak Bay. This passage is 15 km wide and 30 km long; it gradually ascends from an elevation of 15 m at Iliamna Lake to 150 m near its middle, then descends to sea level at Kamishak Bay. The gap is flanked north and south by mountains higher than 1000 m. Winds emanating from this gap occur in all seasons, but are most prevalent in late winter and early spring.

Figure 3 shows the Alaska sea level pressure analysis for 00 UTC 11 February 1982. Notable in the analysis are the low pressure system located over the northwest coast of the continental United States, the ridge of high pressure extending southward over the Bering Sea and past the Aleutian Islands, and the wedge of cold air crossing the Alaskan interior and covering the Alaska Peninsula. The accompanying pressure gradient over Cook Inlet is large (1 mb in 25 km) and oriented WNW–ESE, corresponding to a 25 m $s^{-1}$ north-northeasterly geostrophic wind. Given this pressure gradient, the regional geotriptic wind (balance of pressure gradient, Coriolis and friction forces; Johnson 1966) is from the north-northwest at 18 m $s^{-1}$. This computation is corroborated by north-northwesterly winds (in Fig. 3) at King Salmon and over the western Gulf

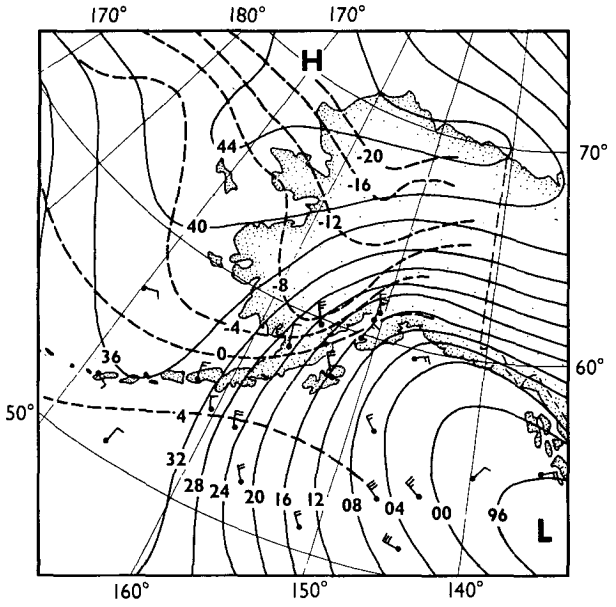


FIG. 3. Alaska sea level pressure analysis for 00 UTC 11 February 1982. High pressure northwest of Alaska and low pressure over the eastern Pacific Ocean caused a steep pressure gradient over Cook Inlet. A reservoir of cold air pooled west of the Aleutian Range. (Solid contours denote pressure in coded mb, dashed lines temperature in °C, full wind barb = 5 m $s^{-1}$.)

of Alaska. As indicated by the wind barbs at Anchorage, Kenai, and Homer, the flow is southward in upper Cook Inlet. Iliamna's surface wind shows a more westerly direction and a speed twice that of King Salmon's. Kodiak's northwest wind is probably a local downgradient wind blowing through a valley upstream of the airport observatory.

The sea level pressure pattern in Fig. 3 is a common winter occurrence. High sea level pressures associated with continental-polar air masses tend to occur over the Alaskan interior while lower sea level pressures accompanied by maritime or modified arctic air masses tend to occur over the Gulf of Alaska. The pressure gradient between these regions is especially steep at mountainous coasts and is enhanced by cyclonic storms propagating into or developing over the Gulf of Alaska.

## 3. Data sources and analysis methods

This study is based on measurements collected by a NOAA P-3 research aircraft on 10 February 1982. The aircraft followed the flight track shown in Fig. 4, departing from and returning to Anchorage on a 7-hour mission. Data gathered during this flight consisted of flight level information from low altitudes (50 and 80 m), a cross section to 440 m, a vertical ascent to dropsonde altitude (3000 m), and radio-telemetry from three Omega dropwindsondes (ODWs). A description of the aircraft, its determination of meteorological variables, instrument calibration, and accuracy are contained in Merceret and Davis (1981) and Merceret et al. (1983). Franklin (1983) describes processing of ODW soundings. We composited these data with hourly surface observations from Anchorage, Kenai, Homer, Iliamna, King Salmon, and Kodiak, and synoptic analyses such as the Alaska and Northern Hemisphere sea level pressure charts.

Aircraft data were sampled at the rate of 1 $s^{-1}$, then averaged over 90-s periods (~9 km). At this period there was a gap between turbulence and mesoscale contributions to the longitudinal wind speed spectrum. Averaged wind speeds and temperatures from 80-m and 50-m altitudes were corrected for small altitude departures from nominal flight level by an iterative technique employing Monin-Obukhov similarity theory (see, for example, Wyngaard 1973) using an empirical relationship (Pierson 1978) of sea surface roughness length to friction velocity for closure. This procedure also yielded estimates of surface fluxes of momentum, sensible and latent heat, and 10-m wind, air temperature, and humidity. Averaged sea level pressure was corrected to the study verification time, 00 UTC 11 February 1982. The correction was made by biasing each aircraft sea level pressure average by the distance-weighted mean of the isallobaric changes at the regional observatories (Kodiak, Homer, King Salmon, etc.) occurring during the interval defined by the aircraft observation time and verification time. Omega dropwindsonde data were block averaged over 30-m layers.

This database allowed construction of mesoscale analyses in three orthogonal planes and budget studies of momentum and heat along the axis of the jet. Horizontal analyses of sea level pressure, 10-m wind speed

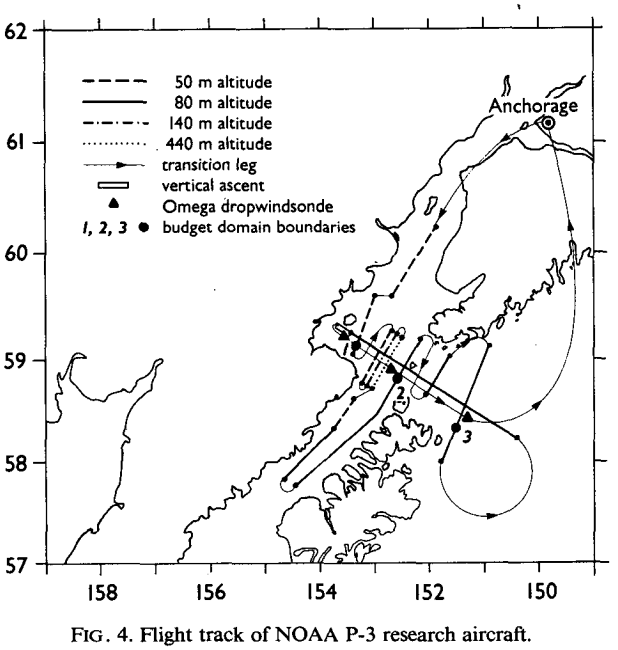


FIG. 4. Flight track of NOAA P-3 research aircraft.

and 10-m potential temperature ($\theta$) were based on low-level flight data. A cross-sectional analysis of wind speed and $\theta$ in a vertical plane normal to the jet ~80 km downstream from the coast was constructed from flight level data at 50, 140, and 440 m. A longitudinal analysis of wind speed, $\theta$, and specific humidity ($q$) in a vertical plane closely parallel to the jet's axis was produced from observations taken during a slow aircraft ascent southwest of Augustine Island and from ODWs launched over Kamishak Bay, the Barren Islands, and the northwestern Gulf of Alaska. In each analysis dashed lines indicate the locations of the analyses in the other two dimensions.

Using these analyses and ancillary flight data, we computed estimates for the budgets of momentum, potential temperature, and equivalent potential temperature ($\theta_e$) for the gap wind.

## 4. Three-dimensional structure of the jet

The horizontal section of sea level pressure and low-level vector wind (Fig. 5a) shows a ridge of high pressure collocated with a jet of air projecting eastward from the Kamishak gap into lower Cook Inlet. The pressure ridge and jet were still distinguishable 230 km downstream from the gap. The pressure perturbation associated with the jet amounted to 2 mb near the coast, decreasing to less than 1 mb offshore where the jet began to merge with the ambient flow in the Gulf. The width of the ridge increased with fetch, and, in an average sense, the pressure gradient decreased with fetch. Asymmetry in the sea level pressure field about the axis of the ridge was probably caused by topographic effects. The 80-m wind vectors show a zone of abrupt wind shift along the northeastern boundary of the jet. Lateral jet boundaries were readily discernible to flight personnel by the change in the intensity of air turbulence. The water surface below the jet was wildly disturbed by whitecaps and foam streaks indicative of strong wind over short fetch.

The 10-m wind speed analysis (Fig. 5b) shows that the highest speeds within the jet (>20 m $s^{-1}$) occurred slightly to the southwest of the ridge axis and ~90 km downstream of the coast at Kamishak Bay. Some acceleration seaward of the coast can be attributed to the reduced drag of the water surface compared with that of land. Under modeled rough-to-smooth and cold-to-warm transitions at the edge of the Bering Sea ice pack, for example, acceleration occurs from 15 km upwind to 40 km downwind of the roughness/thermal discontinuity (Overland et al. 1983). The acceleration in the present case is at least partially due to the orography. The terrain along the boundaries of the jet, especially along the southwest boundary from Kamishak Bay to Cape Douglas, inhibited the adjustment of the mass and velocity fields towards geostrophic balance (Overland 1984). Consequently, the flow continued strongly down the pressure gradient a considerable distance greater than the local Rossby radius (~50 km). A more quantitative analysis of the dynamics of the low-level jet is presented in the following section.

Thermally the jet was characterized by cold air streaming through Kamishak gap (Fig. 5c). Upon leaving the gap the jet began to warm, widen, and deepen through entrainment of warmer ambient air and upward-directed heat flux from the inlet below. Along-axis warming at 10-m altitude amounted to about 1°K per 40 km of fetch.

Coriolis deflection of the flow is evident in all three horizontal sections. Flow features curved to the right and winds became more geostrophic with fetch. The transit time for air parcels traveling along the axis from the coast to 200 km offshore was ~3 h.

Figures 5a,b show that low-level wind speeds > 20 m $s^{-1}$ accompanied by weak ridging were also present in Shelikof Strait. This region of high wind speeds was bordered by regions of weaker winds and warmer low-level temperatures (Fig. 5c) within Shelikof Strait. As the terrain upstream is relatively low and includes two river valleys, it is likely that the high speeds here were also a result of a mountain-gap phenomenon.

The cross section in Fig. 6 shows characteristics of the lower portion of the Kamishak mountain-gap wind near the center of lower Cook Inlet. The cold core of the jet extends from just above the surface to 400 m. The structure appears asymmetric with the fastest winds on the southwest side of the coldest temperatures. A surface layer characterized by superadiabatic lapse rates is evident; the trend of surface-layer heights increasing to the southwest is consistent with estimates of the Obukhov length. The horizontal temperature gradient was also greater on the southwest side of the jet. This asymmetry may result from the bounding orography on the southwest side.

The longitudinal section (Fig. 7) describes wind velocity, $\theta$, and $q$ of the jet and the lower troposphere to an altitude of 3 km. The upstream and central ODWs used in this section were deployed very near the jet's axis, but the downstream ODW was released ~25 km northeast of the axis. Four distinct layers are shown based on the vertical wind shear and stratification. The uppermost layer, above the bold line at ~2000 m, is the free atmosphere. It is statically stable and presumably in gradient-wind balance. Below it (between the bold and bold dashed lines) is a layer that is less stably stratified. Strong northerlies were found in this layer at the location of the central and downstream (southeastern) ODWs. The upstream ODW measured weak northeasterlies. This wind direction is colinear with the orientation of upper Cook Inlet. We surmise that this layer is the upper Cook Inlet boundary layer displaced vertically by the denser gap wind below. During the flight observers noted a cloud patch at 1000 m about 80 km downstream from Kamishak Bay. This feature corresponded to the location of maximum $q$ in the longitudinal section.

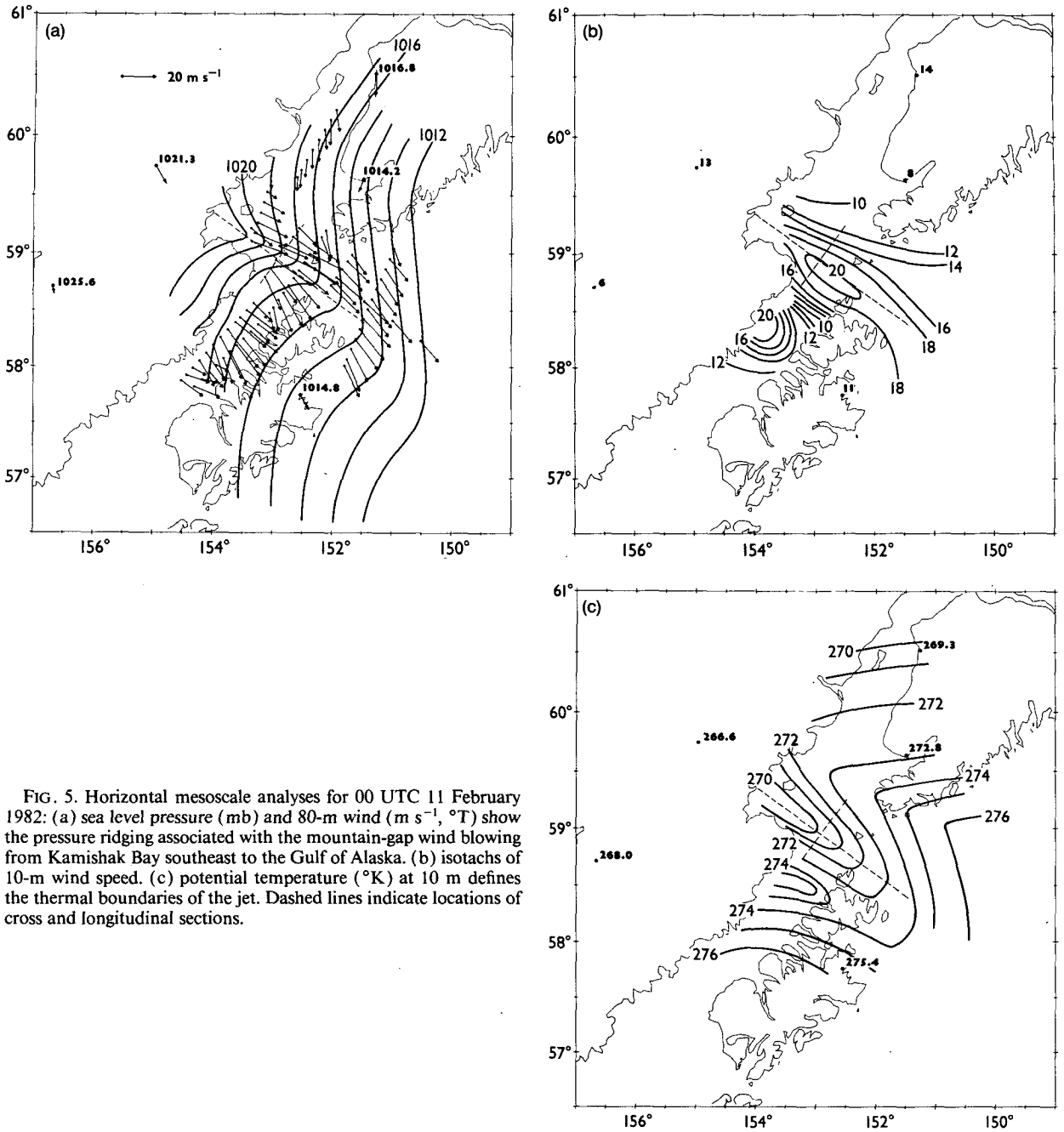


FIG. 5. Horizontal mesoscale analyses for 00 UTC 11 February 1982: (a) sea level pressure (mb) and 80-m wind (m $s^{-1}$, °T) show the pressure ridging associated with the mountain-gap wind blowing from Kamishak Bay southeast to the Gulf of Alaska. (b) isotachs of 10-m wind speed. (c) potential temperature (°K) at 10 m defines the thermal boundaries of the jet. Dashed lines indicate locations of cross and longitudinal sections.

The next lowest layer (between the dashed and dash-dotted lines) represents a transition layer between the lifted Cook Inlet boundary layer and the low-level jet. This layer was about 500 m deep and featured greater static stability and more vertical wind shear than the layers above and below. The transition layer was relatively dry and had northwesterly winds at the upstream ODW, suggesting that it had passed over the Alaskan peninsula (but wasn't accelerated through the Kamishak Gap). The transition layer at the other two ODWs was more moist and had more northerly winds.

The bottom layer (beneath the dash-dotted line) represents the jet with a depth of 300 m at the upstream ODW and 380 m at the downstream ODW. The winds (based on flight-level measurements at 80 m) increased from the upstream to the central ODW site then decreased. The $\theta$ and $q$ of the jet increased with fetch. As shown also by the cross section, the surface layer became deeper and less statically unstable with fetch as the air–sea temperature difference decreased. Above the superadiabatic portion the rest of the layer was adiabatic. This adiabatic layer probably had finite thick-

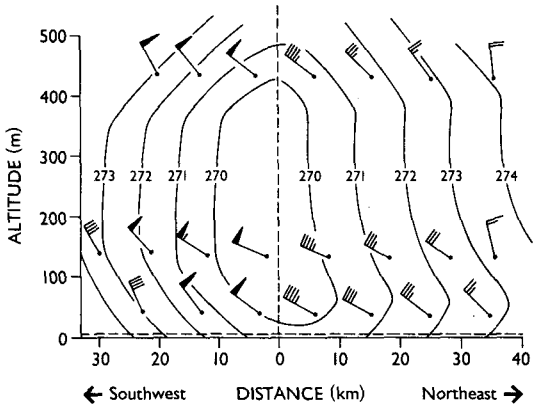


FIG. 6. A low-level cross section of horizontal wind (full barb = 5 m $s^{-1}$, direction in °T), and potential temperature (K) versus altitude (m) and distance (km) across the jet axis from southwest to northeast indicates the asymmetry, wind shear and cold core of the mountain-gap wind. Dashed lines indicate locations of horizontal and longitudinal sections.

ness upstream of Kamishak Bay because of mechanical mixing. Formation of the superadiabatic layer likely began with passage over the relatively warm surface of Kamishak Bay.

## 5. Budgets of momentum and heat for the jet

Our aircraft observations revealed the detailed structure of the low-level jet, which included some surprises. For example, the strongest 10-m winds (Fig. 5b) were found ~90 km downstream of Kamishak gap even though the low-level flow continued strongly down the pressure gradient for at least another 100 km. We sought to explain this observation, along with other characteristics of the jet, by evaluating budget equations. Our principal goal was to determine if a simple treatment of the physics could account for the salient features of the flow.

### *a. Method*

We calculated terms of the momentum, $\theta$, and $\theta_e$ equations following the flow along the axis of the low-level jet. Budget terms were computed as averages over the depth of the jet, as this was an environment of neutral or negative static stability, and vigorous vertical mixing was occurring. We separated the analysis domain into an upstream portion and a downstream portion of the jet (Fig. 4) and calculated budgets for each region separately as well as for the whole domain. The common point of these two regions was just southeast of the launch location of the middle ODW, ~100 km downstream from Kamishak gap. The low-level jet's speed increased by 5% and its thickness grew by 20% along the upstream section. Wind speed and thickness were near constant along the downstream section.

The equation for momentum in the direction of motion of the low-level jet is written as

$$\frac{du}{dt} = \frac{-1}{\rho}\frac{\partial p}{\partial x} + \frac{1}{\rho}\frac{\partial \tau_{zx}}{\partial z} + \frac{1}{\rho}\frac{\partial \tau_{yx}}{\partial y}, \qquad (1)$$

where $u$ is the depth-averaged wind speed, the $x$-direction is parallel to the flow, the $y$-direction is normal to the flow (pointing to the left facing downstream), and $\tau_{zx}$ and $\tau_{yx}$ are stresses acting on a horizontal plane (constant $z$) and a vertical plane (constant $y$), respectively, in a direction parallel to the flow. This coordinate

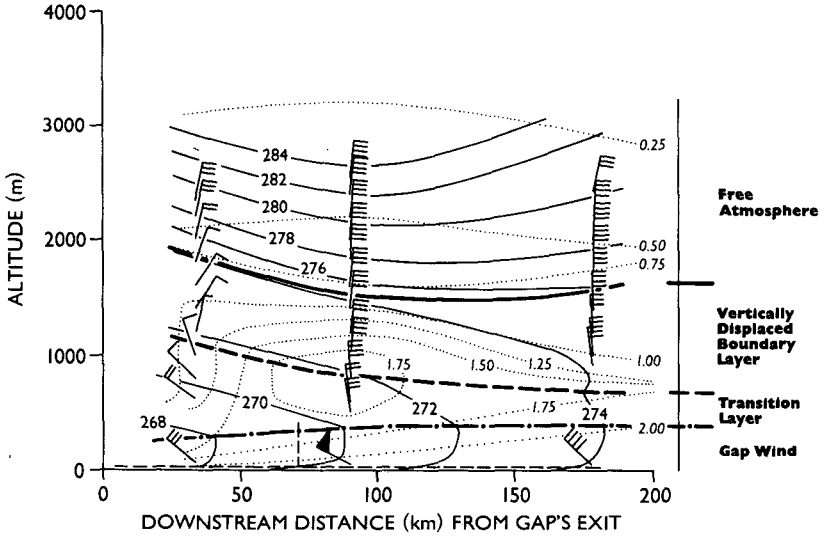


FIG. 7. Longitudinal section of horizontal wind (full barb = 5 m $s^{-1}$, °T), potential temperature (K) and specific humidity versus altitude (km) and distance (km) downstream from the end of Kamishak gap. Vertical lines indicate locations of dropwindsondes; bold lines divide specific layers. Dashed lines show locations of horizontal and cross sections.

system curves to follow the flow; the Coriolis force is implicit, at any particular location it is directed to the right of the flow and does not affect the flow's magnitude. In a manner similar to Lackmann and Overland (1989), (1) is averaged over depth and linearized over the length of each section. We assume incompressibility and neglect the mean advections of momentum in the vertical and cross-jet directions. Remaining on the lhs of (1) are terms representing the Lagrangian tendency; the local rate of change of momentum and the horizontal advection of momentum in the downstream direction. The stress divergence in the vertical is computed from estimates of the surface friction and the vertical entrainment at the top of the jet. These effects are kept separate in the budget tabulations that follow. The stress divergence in the horizontal (cross stream) direction is calculated from estimates of the lateral entrainment along the northeastern boundary of the jet. The momentum equation can now be written in the form

$$\frac{\partial \bar{u}}{\partial t} + \frac{(\bar{u}_f^2 - \bar{u}_i^2)}{2L} = \frac{1}{\rho}\frac{(\bar{p}_i - \bar{p}_f)}{L} + \frac{\overline{w'u'}_s}{H} - \frac{\overline{w'u'}_t}{H} - \frac{\overline{v'u'}_b}{l}. \quad (2)$$

Here, the $i$ subscript refers to a value at the initial (upstream) boundary of the section, subscript $f$ refers to the final (downstream) boundary, $L$ is the horizontal length of the section, $l$ is the average horizontal half-width of the jet, $H$ is the average depth of the jet, and overbars refer to section averages. The stresses are expressed in terms of turbulent fluxes of momentum and the $s$, $t$, and $b$ subscripts refer to fluxes at the surface, top and northeastern boundary of the jet, respectively.

The equation for $\theta$ following the axis of the low-level jet can be written as

$$\frac{d\theta}{dt} = \frac{-1}{\rho}\frac{\partial}{\partial z}E_{hz} - \frac{1}{\rho}\frac{\partial}{\partial y}E_{hy}, \quad (3)$$

where $E_{hz}$ and $E_{hy}$ are the mean vertical and cross-stream turbulent fluxes of $\theta$. Radiational effects and latent heating are neglected. Linearizing and averaging over the sections, (3) can be converted to

$$\frac{\partial \theta}{\partial t} + \frac{(\bar{u}_f + \bar{u}_i)(\theta_f - \theta_i)}{2L} = \frac{\overline{w'\theta'_s}}{H} - \frac{\overline{w'\theta'_t}}{H} - \frac{\overline{v'\theta'_b}}{l}. \quad (4)$$

Again, turbulent fluxes due to surface heating, vertical entrainment, and lateral entrainment were estimated separately. An identical equation was developed for $\theta_e$.

Our budget calculations require wind and thermodynamic data over the depth of the low-level jet, yet our observations were concentrated near 50 and 80 m within the surface layer. At points of computation of budget terms, lapse rates of thermodynamic properties from the closest ODW were used to estimate depth-averaged quantities from surface-layer observations. The ODWs did not yield wind observations below ~700 m, but a single boundary-layer wind profile was available from a vertical ascent by the aircraft. Based on this profile, the average wind speed over the depth of the jet was estimated by applying a constant multiplier of 1.2 to the 10-m winds deduced from aircraft legs at 50 and 80 m.

Aircraft observations within the surface layer (near either 50 or 80 m) allowed estimation of wind speeds, pressures, and values of $\theta$ and $\theta_e$ at the end points of each section. We computed surface fluxes by the bulk aerodynamic technique, incorporating stability-corrected and wind-dependent transfer coefficients. Data selected were centered at the axis of maximum wind speed. Quantities representing averages over depth within the jet were estimated using the technique outlined above. The ODW soundings near the end points of each section were used to determine the depth of the low-level jet and to estimate the vertical entrainment fluxes at the top of the jet.

These entrainment fluxes could only be calculated indirectly. Their importance is suggested by the ODW and flight-level data which shows that the low-level jet deepened (Fig. 7) and widened (Fig. 5a) significantly with fetch. It is plausible that the entrainment of low-momentum air at the lateral and upper boundaries of the jet represented a significant retarding force and heating source. Following Lackmann and Overland (1989) we evaluated a conservation equation for the height of the low-level jet of the form

$$\frac{dH}{dt} = w_e + \bar{w}, \quad (5)$$

where $w_e$ is the vertical entrainment velocity and $\bar{w}$ is the average vertical velocity at the top of the jet. This formulation implies that the top of the low-level jet is a quasi-material surface. Assuming steady-state conditions (5) can be rewritten as

$$u\frac{\partial H}{\partial x} = w_e - \bar{H}\left(\frac{\partial u}{\partial x} + \frac{\partial v}{\partial y}\right). \quad (6)$$

We computed $w_e$ as a residual using estimates of all other terms in (6).

The vertical entrainment fluxes of momentum, $\theta$ and $\theta_e$ were then estimated, following Lilly (1968) using

$$\overline{w'u'_t} = -w_e\Delta u, \quad (7)$$

$$\overline{w'\theta'_t} = -w_e\Delta\theta, \quad (8)$$

and

$$\overline{w'\theta'_{et}} = -w_e\Delta\theta_e. \quad (9)$$

In these equations, $\Delta u$, $\Delta\theta$, and $\Delta\theta_e$ are changes in the wind-speed, $\theta$, and $\theta_e$, respectively, across a transition layer separating the low-level jet from the Cook Inlet boundary layer flow. The thickness of the transition layer is 500 m based on the vertical shear and ther-

modynamic profiles from the ODWs. The entrainment formalism expressed by (7), (8), and (9) was developed for the limiting case of an infinitesimally thin inversion layer capping a well-mixed boundary layer; we extend its application here.

An estimate for the lateral entrainment follows from a parallel argument. A conservation equation for the half-width of the jet ($l$) can be written as

$$\frac{dl}{dt} \approx u_l \frac{\partial l}{\partial x} \approx v_e + \bar{v}, \qquad (10)$$

where $u_l$ is the velocity averaged across the half-width of the jet, $v_e$ is the lateral entrainment velocity, and $\bar{v}$ is the mean velocity component orthogonal to the jet's lateral boundary. A steady-state assumption has been used to reduce the Lagrangian change in $l$ to a single term, the along-flow advection of $l$. We determined $l$ from the flight level winds, which showed distinct changes in wind speed and direction at the boundaries of the jet (Fig. 5a), and from standard deviations in the 90-s averages of vertical velocity. As with the vertical entrainment fluxes the lateral entrainment fluxes of $u$, $\theta$, and $\theta_e$ at the boundary of the jet are estimated as the products of $v_e$ and the changes $\delta u$, $\delta\theta$, and $\delta\theta_e$, respectively, across a transition region (assumed 25 km wide based on inspection of aircraft data measured at the jet's boundaries) at the boundary of the jet. The lateral turbulent fluxes at the axis of the jet are assumed to be zero, and the flux divergencies at this axis are assumed to be equal to their average values over the half-width of the jet. Errors may be introduced by this method of estimating turbulent fluxes.

Budget values determined for the gap-wind layer are sensitive to the techniques used in data processing and analysis. For relative changes in observed parameters over the budget domain, we believe that errors introduced by averaging and interpretation are greater than those arising from instrument error. Flight level data, sampled at 1 $s^{-1}$, were block-averaged over 90 s. Application of secondary-circulation scaling ($L \propto 2H$) suggested that there were 12 independent samples in each averaging interval. The uncertainty associated with the average of each flight-level variable was estimated using the variable's standard deviation and a two-tailed Student's $t$-test ($n < 30$) at the 95% confidence level. Our ability to interpret vertical and lateral distance scales, $H$ and $l$, was, of course, no more accurate than the averaging intervals (30 m and 9 km, respectively), and we have assumed these as error bounds. To estimate uncertainty in vertical and lateral shear, we used twice the indicated error in the flight-level wind. Other variables were treated similarly. Uncertainties in each of the budget terms were determined from the worst-case combination of contributing variables.

### b. Results

The observations and uncertainties used for the budget calculations are summarized in Table 1. Points, 1, 2, and 3 (Fig. 4) refer to the upwind, central, and downwind locations of our analysis domain. As discussed earlier, Table 1 shows that the wind speeds along the axis of the jet were near constant as the jet flowed down gradient ($\Delta p \approx 5.5$ mb). The $\theta$ and $\theta_e$ values of the jet increased with fetch, although surprisingly, $\theta$ increased faster than $\theta_e$ along the upstream section between points 1 and 2, meaning that the specific humidity ($q$) decreased with fetch. The surface fluxes of sensible and latent heat were greatest at point 2 largely because the sea surface temperature increased with fetch along the upstream section. Uncertainties associated with the surface fluxes were ~30% to ~60% of the dominant terms in the respective budgets.

Terms used to estimate the entrainment fluxes are summarized in Table 2. The vertical entrainment velocity was found to be $\sim 7 \times 10^{-2}$ m $s^{-1}$ along the upstream section and $\sim 5 \times 10^{-2}$ m $s^{-1}$ along the

TABLE 1. Values and uncertainties of terms used for budget calculation.

| | Midlayer parameters | | | | Surface fluxes | | |
|---|---|---|---|---|---|---|---|
| Location | $\bar{p}$ (mb) | $\bar{u}$ (m $s^{-1}$) | $\bar{\theta}$ (K) | $\bar{\theta}_e$ (K) | $\tau$ (N $m^{-2}$) | $E_{hs}(\theta)$ (W $m^{-2}$) | $E_{hs}(\theta_e)$ (W $m^{-2}$) |
| 1 | 1020.8 ± 0.4 | 22.8 ± 3.0 | 268.8 ± 0.2 | 274.4 ± 0.2 | 0.9 ± 0.4 | 145 ± 55 | 325 ± 120 |
| 2 | 1017.2 ± 0.1 | 23.8 ± 2.0 | 270.8 ± 0.2 | 275.2 ± 0.4 | 1.0 ± 0.4 | 265 ± 85 | 650 ± 205 |
| 3 | 1015.3 ± 0.2 | 23.2 ± 1.5 | 272.8 ± 0.1 | 279.2 ± 0.2 | 0.9 ± 0.3 | 175 ± 50 | 475 ± 135 |

| | Vertical parameters | | | | Lateral parameters | | | | |
|---|---|---|---|---|---|---|---|---|---|
| | $H$ (m) | $\Delta u$ (m $s^{-1}$) | $\Delta\theta$ (K) | $\Delta\theta_e$ (K) | $l$ (km) | $u_l$ (m $s^{-1}$) | $\delta u$ (m $s^{-1}$) | $\delta\theta$ (K) | $\delta\theta_e$ (K) |
| 1 | 300 ± 30 | −11 ± 6 | 4 ± 0.3 | 3 ± 0.5 | 18 ± 9 | 20.9 ± 3.0 | −18 ± 6 | 3 ± 0.3 | 4 ± 0.5 |
| 2 | 370 ± 30 | 0 ± 4 | 3 ± 0.3 | 3 ± 0.8 | 24 ± 9 | 22.8 ± 2.0 | −8 ± 4 | 2 ± 0.3 | 2 ± 0.8 |
| 3 | 380 ± 30 | 1 ± 3 | 1 ± 0.2 | −2 ± 0.4 | 29 ± 9 | 22.0 ± 1.5 | −7 ± 3 | 2 ± 0.2 | 0 ± 0.4 |

TABLE 2. Values and uncertainties of terms used to estimate entrainment fluxes.

| Region | $L$ (km) | $\bar{w}$ (cm s$^{-1}$) | $w_e$ (cm s$^{-1}$) | $v_e$ (m s$^{-1}$) |
|---|---|---|---|---|
| 1 → 2 | 54 | −3.6 ± 5.7 | 6.7 ± 7.4 | 2.4 ± 8.4 |
| 2 → 3 | 82 | −4.9 ± 3.9 | 5.2 ± 4.9 | 1.4 ± 5.4 |
| 1 → 3 | 136 | −4.4 ± 2.4 | 5.8 ± 3.1 | 1.8 ± 3.4 |

downstream section. A relatively larger value would be expected for $w_e$ along the upstream section, as this region had both surface buoyancy and transition-layer shear as sources of turbulence to drive vertical entrainment (Stull 1976), while the downstream section had only surface buoyancy. Assuming that the entrainment flux of buoyancy along the downstream section was 0.2 times the surface flux of buoyancy (Stull 1976) yields an entrainment rate estimate of $\sim 2 \times 10^{-2}$ m s$^{-1}$, the same order of magnitude as our estimate. The lateral entrainment rate was an average of $\sim 2$ m s$^{-1}$. Computations of $w_e$ and $v_e$ are especially sensitive to the relatively large uncertainty in $\bar{u}$ (Table 1). Therefore, entrainment rate uncertainties are of the order of the rates themselves.

The budget calculations and uncertainties are tabulated in Table 3. The residuals, the rightmost column of Table 3, are expressed as differences between the total forcing and the Lagrangian changes. Figure 8 summarizes the budgets for the domain as a whole (that region defined by point 1 to point 3 in Fig. 4). The momentum budgets show that the Lagrangian changes were minimal. The principal balance was between the retarding effect of surface friction and the acceleration due to the pressure gradient. Lateral and vertical entrainment were secondary retarding effects. As discussed above, the vertical entrainment rate is probably underestimated for the downstream section and for the domain as a whole, but the relative magnitudes of these errors on the momentum budgets appear to be small.

The $\theta$-budget results show that the Lagrangian changes in $\theta$ were large due principally to the advection terms. This cold advection was balanced by the surface heat flux, vertical entrainment and to a lesser extent, by the lateral entrainment flux. The residuals for the $\theta$ budgets were of the order of half of the advection terms.

The surface fluxes were the dominant effects opposing the advection terms in the budgets for $\theta_e$. The vertical entrainment of $\theta_e$ was more important than the lateral entrainment for the domain as a whole (Fig. 8), but both processes were secondary. The vertical entrainment of $\theta_e$ was smaller than the vertical entrainment of $\theta$ because the air above the jet was drier as well as potentially warmer. The residual in the $\theta_e$ budget for the upstream section was large. The advection of $\theta_e$ was relatively small along this section because of the decrease in $q$ with fetch. This result is physically implausible as there was such strong surface flux of latent heat in this region. We suspect that the flight track intercepted nonrepresentative air parcels yielding either an overestimate of $q$ at point 1 or an underestimate of $q$ at point 2 or both. As the residual in the $\theta_e$ budget between points 2 and 3 is small, it is more likely that the $q$ at point 1 was overestimated. If so, the advection of $q$ (and $\theta_e$) was greater than shown in Table 3. In support of this conjecture the longitudinal section (Fig.

TABLE 3. Budget terms and uncertainties.

Momentum budgets (in $10^{-3}$ m s$^{-2}$)

| Region | Local change | Horizontal advection | Pressure gradient | Surface friction | Entrainment: Vertical | Entrainment: Lateral | Residual |
|---|---|---|---|---|---|---|---|
| 1 → 2 | −0.2 ± 0.5 | 0.4 ± 2.1 | 5.0 ± 0.7 | −2.1 ± 1.2 | −1.1 ± 3.7 | −1.5 ± 14.8 | 0.1 |
| 2 → 3 | −0.3 ± 0.5 | −0.2 ± 1.0 | 1.8 ± 0.3 | −2.0 ± 0.9 | 0 ± 1.1 | −0.4 ± 3.8 | −0.1 |
| 1 → 3 | −0.3 ± 0.5 | 0.1 ± 0.7 | 3.1 ± 0.3 | −2.0 ± 1.0 | −0.4 ± 1.0 | −0.8 ± 4.6 | 0.1 |

$\theta$ Budgets (in $10^{-4}$ °K s$^{-1}$)

| Region | Local change | Horizontal advection | Surface flux | Entrainment: Vertical | Entrainment: Lateral | Residual |
|---|---|---|---|---|---|---|
| 1 → 2 | 1.2 ± 0.3 | 8.8 ± 2.5 | 4.6 ± 2.2 | 7.0 ± 10.7 | 2.7 ± 21.2 | 4.3 |
| 2 → 3 | 0.9 ± 0.4 | 5.7 ± 1.2 | 4.5 ± 1.9 | 2.8 ± 3.8 | 0.8 ± 6.3 | 1.5 |
| 1 → 3 | 1.0 ± 0.3 | 6.8 ± 1.2 | 4.5 ± 2.0 | 4.4 ± 2.8 | 1.6 ± 5.9 | 2.7 |

$\theta_e$ Budgets (in $10^{-4}$ °K s$^{-1}$)

| | | | | | | |
|---|---|---|---|---|---|---|
| 1 → 2 | 0.9 ± 0.6 | 3.3 ± 3.4 | 11.0 ± 5.1 | 6.0 ± 10.8 | 3.1 ± 26.5 | 15.9 |
| 2 → 3 | 1.0 ± 0.8 | 11.5 ± 2.7 | 11.5 ± 4.7 | 0.7 ± 2.5 | 0.4 ± 4.7 | 0.1 |
| 1 → 3 | 1.0 ± 0.5 | 8.1 ± 1.6 | 11.3 ± 4.9 | 2.8 ± 2.1 | 1.4 ± 6.0 | 6.4 |

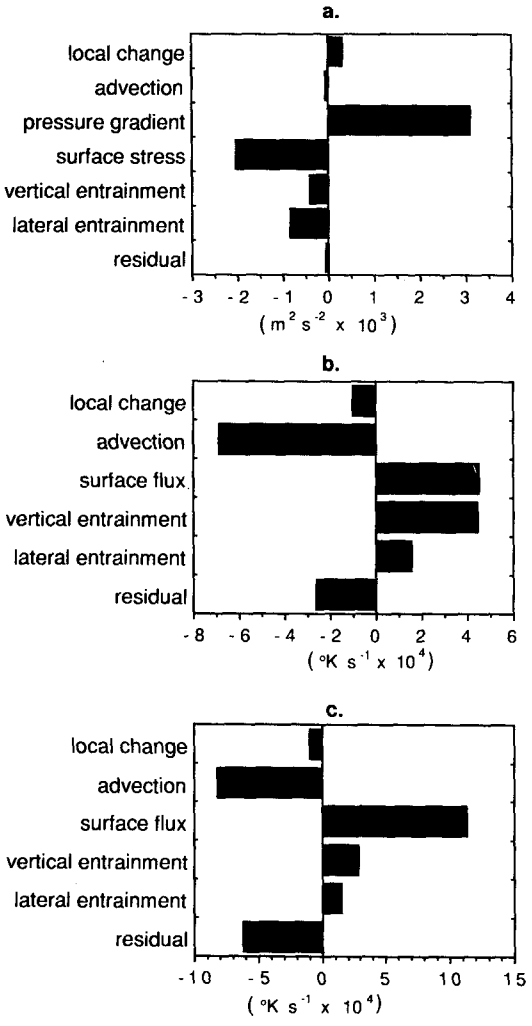


FIG. 8. Budgets of (a) momentum, (b) potential temperature, and (c) equivalent potential temperature for the jet over the whole domain (from point 1 to point 3 in Fig. 4).

7) based on ODW data shows a monotonic increase in $q$ with fetch.

In all the budgets the greatest uncertainties were associated with the entrainment terms. They are large because of the sensitivity of the rate equations (6) and (10) to gustiness in the gap wind. Note, however, that in all budgets except the $\theta$ and $\theta_e$ budgets for the upstream section the entrainment uncertainties are less than the primary forcing.

Some general conclusions can be drawn from these budgets. The momentum budget revealed that the Lagrangian change in momentum was small in the presence of a substantial pressure gradient along the flow. The surface stress was the dominant retarding effect. This can be attributed in part to the high initial wind speeds (recall that the surface winds were 15 m $s^{-1}$ at Iliamna before the flow had reached the water). Since the jet was shallow, the divergence in the surface stress (and the stress at the top of the jet) were relatively large. In the $\theta$ budget the effects of the surface and vertical entrainment heat fluxes were large because the jet was shallow. The acceleration and warming of these types of flows are strongly related to their initial depth.

The sea level pressure gradient parallel to the flow was greater in the upstream (nearshore) portion of the analysis domain (Table 3). Most of this decrease with fetch can be attributed to the process of geostrophic adjustment, i.e., the flow became more parallel to the isobars farther downstream. Given the magnitude of surface friction, a slight deceleration of the low-level flow in the downstream portion of the domain would be expected. The absolute magnitude of the sea level pressure gradient also decreased with fetch partly because the low-level temperature gradient associated with the jet decreased with fetch. In addition cold-air damming by the high terrain of the Alaskan peninsula and southern Alaska mainland appears to have resulted in a regional sea level pressure gradient that was stronger along the coast than farther offshore.

Lackmann and Overland (1989) found different results for the case of a gap wind flowing down the pressure gradient in Shelikof Strait. In their case vertical entrainment was more important than surface friction in the along-strait momentum budget while in their along-strait $\theta_e$ budget, vertical entrainment was about half as important as surface heat flux. Their gap wind was deeper than the jet studied here and their case featured less cold advection, lower wind speeds, and greater wind speed acceleration. Their case also exhibited a greater degree of shear across the transition layer capping the gap wind. An increase in shear enhances both the entrainment rate and the momentum flux for a given entrainment rate.

## 6. Summary

The large-scale weather pattern over Alaska often produces mountain-gap winds blowing from the west side of the Alaska Peninsula to the east side through passes and valleys in the mountains of the Aleutian Range. When the reservoir of air behind the Aleutian Range is cold relative to surface air in Gulf of Alaska coastal regions, the mountain-gap winds are significantly colder and denser than ambient surface air. These winds are hazardous to mariners and aviators because of the shear associated with their boundaries, their turbulence intensity, and their ability to cause rough sea states and superstructure icing. Over lower Cook Inlet the gap wind continues to accelerate beyond the coast. This phenomenon may, in part, explain the more-frequently-than-annual occurrence of northwesterly winds in excess of 50 m $s^{-1}$ over the Barren Islands (G. L. Hufford, NWS Anchorage WSFO, personal communication).

On 11 February 1982 a research aircraft made a study of such a wind jet blowing from the Kamishak

gap across lower Cook Inlet. Dense air associated with the jet formed a local pressure ridge which could be traced 200 km downstream of the gap. The jet exhibited lateral asymmetry probably because of an extension of the mountainous coast on the jet's south side. The fastest surface winds, in excess of 20 m $s^{-1}$, were found just to the right of the jet's thermal axis and 90 km downstream of the end of the gap. Upstream of this wind maximum the jet flowed almost directly down the sea level pressure gradient. Downstream, curvature of the flow became more evident presumably due to the Coriolis effect as the wind approached geotriptic balance. A momentum budget revealed that the pressure-gradient force was balanced principally by surface friction. The $\theta$ budget showed largely a balance between the horizontal advection of colder air and the combination of the turbulent fluxes of sensible heat at the surface and the top of the jet. In both the momentum and thermal budgets lateral entrainment fluxes were of secondary importance. The $\theta_e$ budget showed a balance between horizontal advection and surface fluxes of latent and sensible heat. Suggested scales for a Kamishak Gap wind arising from this particular synoptic situation are: length ~200 km, width ~30 km, depth ~500 m, and speed ~1.0 geostrophic.

*Acknowledgments.* The authors express thanks to personnel of NOAA's Office of Aircraft Operations for their willingness to make these important measurements under the hazardous conditions which they represent. We thank the Ocean Service Unit of the Anchorage NWS Forecast Office for their cooperation in preparing and executing this research. The manuscript was enriched through consultation with J. E. Overland, J. Gray, and M. Shapiro.

This article is also a contribution to the Marine Services Program at NOAA's Pacific Marine Environmental Laboratory and is Contribution FOCI-0039 to the Fisheries-Oceanography Coordinated Investigations.

## REFERENCES

Franklin, J., 1983: Omega dropwindsonde processing. NOAA Tech. Memo, ERL AOML-54, 34 pp.

Huschke, R. E., Ed., 1959: *Glossary of Meteorology.* Amer. Meteor. Soc., 638 pp.

Johnson, W. B., Jr., 1966: The "geotriptic" wind. *Bull. Amer. Meteor. Soc.*, **47,** 982.

Lackmann, G. M., and J. E. Overland, 1989: Atmospheric structure and momentum balance during a gap wind event in Shelikof Strait, Alaska. *Mon. Wea. Rev.*, **117,** 1817–1833.

Lilly, D. K., 1968: Models of cloud-topped mixed layers under a strong inversion. *Quart. J. Roy. Meteor. Soc.*, **94,** 292–309.

Macklin, S. A., R. W. Lindsay and R. M. Reynolds, 1980: Observations of mesoscale winds in an orographically dominated estuary—Cook Inlet, Alaska. *Proc. Second Conf. Coastal Meteorology,* Los Angeles, Amer. Meteor. Soc., 176–180.

——, J. E. Overland and J. P. Walker, 1984: Low-level gap winds in Shelikof Strait. *Proc. Third Conf. Meteorology of Coastal Zone,* Miami, Amer. Meteor. Soc., 97–102.

Merceret, F. J., and H. W. Davis, 1981: The determination of navigational and meteorological variables measured by NOAA/RFC WP3D aircraft. NOAA Tech. Memo. ERL RFC-7, 21 pp.

——, R. J. DeVivo, H. W. Davis and J. R. Parrish, 1983: Calibration of meteorological measurements made by NOAA WP3D aircraft—1983. NOAA Tech. Memo. OAO 1, 48 pp.

Overland, J. E., 1984: Scale analysis of marine winds in straits and along mountainous coasts. *Mon. Wea. Rev.*, **112,** 2530–2534.

——, R. M. Reynolds and C. H. Pease, 1983: A model of the atmospheric boundary layer over the marginal ice zone. *J. Geophys. Res.*, **88,** 2836–2840.

——, and B. A. Walter, Jr., 1981: Gap winds in the Strait of Juan de Fuca. *Mon. Wea. Rev.*, **109,** 2221–2233.

Pierson, W. J., 1978: Verification procedures for SEASAT measurements of the vector wind with the SASS. Report to Jet Propulsion Laboratory Contract No. 9554411. [NTIS No. AD-A0703644/7ST.]

Reed, T. R., 1931: Gap winds of the Strait of Juan de Fuca. *Mon. Wea. Rev.*, **59,** 373–376.

Scorer, R. S., 1952: Mountain-gap winds; a study of surface wind at Gibraltar. *Quart. J. Roy. Meteor. Soc.*, **78,** 53–61.

Smith, R. B., 1987: Aerial observations of the Yugoslavian bora. *J. Atmos. Sci.*, **44,** 269–297.

Stull, R. B., 1976: The energetics of entrainment across a density interface. *J. Atmos. Sci.*, **33,** 1260–1267.

Wyngaard, J. C., 1973: On surface-layer turbulence. *Workshop on Micrometeorology,* D. Haugen, Ed., Amer. Meteor. Soc., 101–148.